

Laser-induced charge and spin photocurrents at the BiAg₂ surface: A first-principles benchmark

T. Adamantopoulos ^{1,2,*} M. Merte ^{1,2,3} D. Go ^{1,3} F. Freimuth ^{3,1,†} S. Blügel ¹ and Y. Mokrousov ^{1,3,‡}

¹Peter Grünberg Institut and Institute for Advanced Simulation, Forschungszentrum Jülich and JARA, 52425 Jülich, Germany

²Department of Physics, RWTH Aachen University, 52056 Aachen, Germany

³Institute of Physics, Johannes Gutenberg University Mainz, 55099 Mainz, Germany

 (Received 31 January 2022; revised 2 September 2022; accepted 21 September 2022; published 18 October 2022)

Here, we report first-principles calculations of laser-induced photocurrents at the surface of a prototype Rashba system. By referring to Keldysh nonequilibrium formalism combined with the Wannier interpolation scheme, we perform first-principles electronic structure calculations of a prototype BiAg₂ surface alloy, which is a well-known material realization of the Rashba model. In addition to the nonmagnetic ground state situation, we also study the case of in-plane magnetized BiAg₂. We calculate the laser-induced charge photocurrents for the ferromagnetic case and the laser-induced spin photocurrents for both the nonmagnetic and the ferromagnetic cases. Our results confirm the emergence of very large in-plane photocurrents as predicted by the Rashba model and are in agreement with previous experimental measurements of THz emission generated at Bi/Ag interfaces. The resulting photocurrents satisfy all the symmetry restrictions with respect to the light helicity and the magnetization direction. We provide microscopic insights into the symmetry and magnitude of the computed currents based on the *ab initio* multiband electronic structure of the system, and scrutinize the importance of resonant two-band and three-band transitions for driven currents, thereby establishing a benchmark picture of photocurrents at Rashba-like surfaces and interfaces. Our work contributes to establishing the interfacial Rashba spin-orbit interaction as a major mechanism for the generation of in-plane photocurrents, which are of great interest in the field of ultrafast and terahertz spintronics.

DOI: [10.1103/PhysRevResearch.4.043046](https://doi.org/10.1103/PhysRevResearch.4.043046)

I. INTRODUCTION

The interest in physics of optical generation and properties of laser-induced currents arising at surfaces and interfaces is steadily rising, owing in part to bright prospects that these currents carry for technological applications. Among the latter, the generation of THz radiation with so-called spintronics THz emitters, which rely on spinorbitronics effects taking place in magnetic bilayers, has come to occupy a prominent place [1,2]. As the sources of THz radiation arising from magnetic bilayers exposed to fs laser pulses, two main mechanisms of parent in-plane charge currents are considered: currents generated via the inverse spin Hall effect in response to laser-ignited superdiffusive spin currents [3–8], and currents generated via the inverse spin-orbit torque in response to the inverse Faraday effect [9–11]. However, the diversity of optically mediated planar interfacial currents is not limited to the aforementioned scenarios. For example, recently it was predicted that charge photocurrents can arise from a time-varying exchange splitting following the laser excitation [12].

Furthermore, it was pointed out that laser-induced charge photocurrents can arise in noncentrosymmetric magnetic bilayers as a result of interfacial spin-orbit interaction (SOI) [13]. This effect was coined as the magnetic photogalvanic effect to distinguish it from the circular photogalvanic effect which appears in noncentrosymmetric nonmagnetic semiconductors [14,15]. Moreover, it was also predicted that laser-induced spin photocurrents can arise at metallic surfaces, both magnetic as well as nonmagnetic [13,16].

As one of the fundamental optical phenomena, photogalvanic effects have been intensively studied in the past and they have gained even more interest in recent years due to their potential applications. However, to date, very little is known about photocurrents emerging at metallic surfaces and interfaces, playing such a central role in THz spintronics. Besides a recent study performed within an effective Rashba model [13], not a single report on first-principles calculations of photocurrents in a Rashba-like system is known to us. This should not be too surprising, given the large numerical effort needed to compute nonlinear effects from *ab initio*, as well as a multitude of discussed sources of photocurrents, whose debated relevance depends on a given system. On the other hand, estimating the relevance of different contributions in a given material from first principles at times requires completely different numerical approaches, which makes such studies barely feasible.

Currently, intrinsic contributions which have been identified behind the generation of nonlinear optical responses are the shift and injection currents [17–20], the Berry curvature

*t.adamantopoulos@fz-juelich.de

†f.freimuth@fz-juelich.de

‡y.mokrousov@fz-juelich.de

dipole (BCD) term [21,22], as well as the semiclassical Jerk [23,24] and ballistic terms [25]. The shift and injection terms are important in gapped materials and, on this front, first-principles calculations were performed, for example, in ferroelectric materials [17,26], semiconductors [18,19], quantum wells [27], and graphene [28]. In metals, the presence of the Fermi surface gives rise to the BCD and semiclassical terms, also referred to as metallic terms. Especially for the BCD, it was proposed that the nonlinear Hall effect can be observed in materials with large Berry curvature stemming from accidental or avoided band crossings such as topological crystalline insulators, two-dimensional transition metal dichalcogenides, and three-dimensional Weyl semimetals [21]. Recently, we developed an *ab initio* scheme to calculate second-order optical response properties within the Keldysh formalism [13,29], successfully applying it to study charge and spin photocurrents in single-layer ferromagnetic Fe₃GeTe₂ [16]. The developed approach is optimal in providing reference values in realistic materials, as it can treat both insulating and metallic systems on equal footing, and it naturally lends itself to including various disorder effects, without the need to distinguish among intrinsic and various extrinsic contributions to the photocurrents explicitly.

In recent years, the study of nonlinear spin photocurrents has gained increasing interest, with several theoretical studies reporting the effect in nonmagnetic noncentrosymmetric systems [26–28]. Recently, a significant effort has been devoted to spin photocurrents from a microscopic perspective of novel materials such as two-dimensional (2D) materials and antiferromagnets [13,16,30–33]. The motivation behind the study of these materials is that they host spin photocurrents which exist without the presence of accompanying charge currents—a property that renders them as prolific candidates for highly efficient technological devices [34]. From the experimental side, there has also been an increasing effort in the assessment of spin photocurrents in recent years [9,35–37]. Three of the most important mechanisms used for the detection of spin photocurrents are the effects of spin accumulation, spin torque, and the inverse spin Hall effect. Within the latter, a spin current has been shown to transform into a charge current, resulting in a consequent THz emission which can be detected experimentally [1,3].

In this work, we choose a prototype metallic Rashba system—BiAg₂ surface alloy [38]—and apply the developed Keldysh methodology to study the properties of charge and spin photocurrents at it from first principles. With this, we aim to provide benchmark values and develop a material-specific theory of photocurrents at metallic magnetic and nonmagnetic Rashba surfaces, which can be used in the future as a reference point by other *ab initio* studies. Specifically, we study the properties of photocurrents in the nonmagnetic ground state and in an in-plane magnetized, by the addition of an exchange field in the nonmagnetic Hamiltonian, which in the manuscript we refer to as the ferromagnetic case, analyzing our results in terms of disorder strength, band filling, and frequency of the light. Apart from confirming the predictions of the Rashba model, we also highlight the importance of the Rashba splitting and exchange interaction in generating the responses stemming from resonant two-band transitions in the ferromagnetic case. As such, we also build an intuition

in the required material parameters for a strong optical response, which is necessary for the engineering of experimental materials and promising applications in the field of ultrafast and THz spintronics. Our work is structured as follows. In Sec. II, we briefly describe the computational methodology, and in Sec. III, we provide structural details and details of first-principles calculations. In Sec. IV A, we address the properties of charge photocurrents in the ferromagnetic case, while in Secs. IV B and IV A, we study the physics of spin photocurrents at the nonmagnetic and magnetic surface, respectively. In Sec. V, we discuss the relevance of different electronic transitions behind the computed photocurrents. Our manuscript ends with a summary in Sec. VI.

II. METHOD

In this work, we calculate the charge and spin photocurrents which arise at second order in the perturbing electric field of a continuous laser pulse of frequency ω by using the expressions which were previously derived in [13] within the framework of the Keldysh formalism. The expression for the second-order charge photocurrents flowing in direction i is [13]

$$J_i = \frac{a_0^2 e I}{\hbar c} \left(\frac{\mathcal{E}_H}{\hbar \omega} \right)^2 \text{Im} \sum_{jk} \epsilon_j \epsilon_k^* \varphi_{ijk}, \quad (1)$$

where the quantity φ_{ijk} has the form

$$\begin{aligned} \varphi_{ijk} = & \frac{2}{a_0 \mathcal{E}_H} \int \frac{d^2 k}{(2\pi)^2} \int d\mathcal{E} \\ & \times \text{Tr} [f(\mathcal{E}) v_i G_k^R(\mathcal{E}) v_j G_k^R(\mathcal{E} - \hbar \omega) v_k G_k^R(\mathcal{E}) \\ & - f(\mathcal{E}) v_i G_k^R(\mathcal{E}) v_j G_k^R(\mathcal{E} - \hbar \omega) v_k G_k^A(\mathcal{E}) \\ & + f(\mathcal{E}) v_i G_k^R(\mathcal{E}) v_k G_k^R(\mathcal{E} + \hbar \omega) v_j G_k^R(\mathcal{E}) \\ & - f(\mathcal{E}) v_i G_k^R(\mathcal{E}) v_k G_k^R(\mathcal{E} + \hbar \omega) v_j G_k^A(\mathcal{E}) \\ & + f(\mathcal{E} - \hbar \omega) v_i G_k^R(\mathcal{E}) v_j G_k^R(\mathcal{E} - \hbar \omega) v_k G_k^A(\mathcal{E}) \\ & + f(\mathcal{E} + \hbar \omega) v_i G_k^R(\mathcal{E}) v_k G_k^R(\mathcal{E} + \hbar \omega) v_j G_k^A(\mathcal{E})]. \quad (2) \end{aligned}$$

In the above expressions, a_0 is the Bohr's radius, e is the elementary charge, I is the intensity of the pulse, \hbar is the reduced Planck constant, c is the light velocity, $\mathcal{E}_H = e^2 / (4\pi \epsilon_0 a_0)$ is the Hartree energy, and ϵ_j is the j th component of the polarization vector of the pulse. With v_i , we label the i th component of the velocity operator, $f(\mathcal{E})$ is the Fermi-Dirac distribution function, and $G_k^{R(A)}$ stand for the retarded (advanced) Green function of the system. The expression for the spin photocurrent J_i^s flowing in direction i with spin polarization along axis s is obtained by replacing the first of the velocity operators v_i in Eq. (2), with the operator of the spin velocity $\{v_i, \sigma_s\}$, and the prefactor $a_0^2 e I / \hbar c$ given by Eq. (1) with the prefactor $-a_0^2 I / 4c$.

The energy-dependent Green function of the system is given by [13]

$$G_k^R(\mathcal{E}) = \hbar \sum_n \frac{|kn\rangle \langle kn|}{\mathcal{E} - \mathcal{E}_{kn} + i\Gamma} \quad \text{and} \quad G_k^A(\mathcal{E}) = [G_k^R(\mathcal{E})]^\dagger, \quad (3)$$

where \mathcal{E}_{kn} is the energy of the state $|kn\rangle$ with band index n and a Bloch vector \mathbf{k} . In order to describe the effect of disorder of the electronic states, the constant lifetime broadening Γ is introduced. The parameter Γ allows us to perform the energy integration in Eq. (2) analytically in the way described in [29].

A circularly polarized pulse propagating in the z direction is described by $\boldsymbol{\epsilon} = (1, \lambda i, 0)/\sqrt{2}$, where $\lambda = \pm 1$ is the helicity. Linearly polarized light along the x or y axis is described by $\boldsymbol{\epsilon} = (1, 0, 0)$ and $\boldsymbol{\epsilon} = (0, 1, 0)$, respectively. The assumed intensity of the pulse is 10 GW/cm^2 , which corresponds to typical values of the fluence of the order of 0.5 mJ/cm^2 for a 50 fs laser pulse [9].

III. COMPUTATIONAL DETAILS

The electronic structure of the BiAg_2 surface was calculated from first principles by considering one layer of the BiAg_2 alloy and using the film mode of the full-potential linearized augmented plane wave FLEUR code [39]. The spin-orbit coupling (SOC) effect was treated within the second-variation scheme [40]. For the exchange and correlation effects, the nonrelativistic Perdew-Burke-Ernzerhof (PBE) [41] functional was used. The in-plane lattice constant was chosen at $a = 9.466 \text{ a.u.}$, while the surface relaxation of the Bi atom was set to $d = 1.61 \text{ a.u.}$ —the values determined from our previous first-principles calculations [42]. Within each unit cell, the Ag atoms are positioned at $(1/3, -1/3, -d/2)$ and $(-1/3, 1/3, -d/2)$, while the Bi atom is positioned at $(0, 0, d/2)$, with respect to the unit lattice vectors $a = \alpha(1/2, \sqrt{3}/2)$ and $b = \alpha(1/2, -\sqrt{3}/2)$. The muffin-tin radii of Bi and Ag atoms were set to 2.80 a.u.^{-1} and 2.59 a.u.^{-1} , respectively. The plane-wave cutoff was set to $K_{\text{max}} = 4.0 \text{ a.u.}^{-1}$ and we used a set of 128 k points in the Brillouin zone for self-consistent calculations. The crystal and electronic structures of the system can be seen in Fig. 1 and they reproduce the ones presented in our previous first-principles calculations in Fig. 1 of Ref. [42]. From the first-principles band structure in Fig. 1(c), the Rashba-like effect of including SOC on the k -dependent band splitting of the states is evident.

Next, by using the WANNIER90 code [43], we obtained maximally localized Wannier functions (MLWFs) which reproduce the first-principles electronic structure up to a frozen window of 2.78 eV above the Fermi energy. The chosen initial projections were sp_2 and p_z orbitals for Bi, while for Ag they were s , p , and d orbitals. In this way, we constructed 44 MLWFs out of 120 Bloch functions (BFs) on a $16 \times 16 k$ mesh.

In a postprocessing step, the interpolated Hamiltonian was constructed out of the previously obtained MLWFs. In Fig. 1(c), we present the comparison between the first-principles and the interpolated band structures, where the perfect agreement up to the level of the frozen window is evident. In its ground state, the system is nonmagnetic, and starting from nonmagnetic MLWFs aided by the matrix elements of Pauli matrices [44], an exchange field of the type

$$H_{\text{ex}} = \frac{\Delta V}{2} \boldsymbol{\sigma} \cdot \hat{\mathbf{n}}(\mathbf{r}), \quad (4)$$

where $\boldsymbol{\sigma}$ are the Pauli matrices and $\hat{\mathbf{n}}(\mathbf{r})$ the unit vector, was applied on the interpolated Hamiltonian in order to make the system ferromagnetic and break the time-reversal symmetry. Following the symmetry analysis performed within the Rashba model and presented in Ref. [13], which predicts a vanishing photosignal for the case of out-of-plane magnetization, we choose the direction of the exchange field to be in-plane along the y axis. The calculated band structure of the ferromagnetic case presented in comparison to the nonmagnetic case is shown in Fig. 1(d). Additional asymmetric splittings of the bands, as well as the shift of the metallic Weyl point of mixed type [45] positioned at $+1 \text{ eV}$, characteristic for the Rashba model, away from the Γ point arising in response to the applied exchange field are clearly visible [38].

In the following, we compute the photocurrents in the system and vary the lifetime broadening Γ in a region of $[0.025, 0.5] \text{ eV}$, the light energy $\hbar\omega$ between $[0.15, 2.5] \text{ eV}$, and we cover an energy region of $[-3, 2.5] \text{ eV}$ around the Fermi energy level \mathcal{E}_F . A $512 \times 512 k$ mesh has proved to be sufficient to obtain converged results. The strength of the exchange field was set at $\Delta V = 0.5 \text{ eV}$.

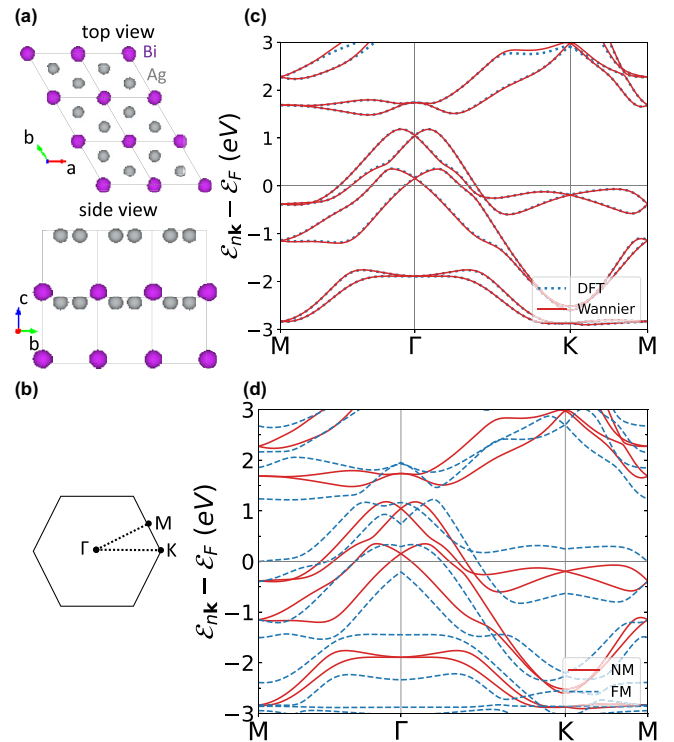


FIG. 1. (a) The crystal structure of the BiAg_2 surface considered in this work shown from a top and side view. (b) The first Brillouin zone and the high-symmetry points. (c) The comparison between the first-principles (DFT, dotted blue line) and the interpolated (Wannier, solid red line) band structures. (d) The interpolated band structure of BiAg_2 around the Fermi energy for the nonmagnetic (NM, solid red line) and the ferromagnetic (FM, dashed blue line) case. For the ferromagnetic case, an exchange field with a strength of 0.5 eV is applied in-plane along the y axis.

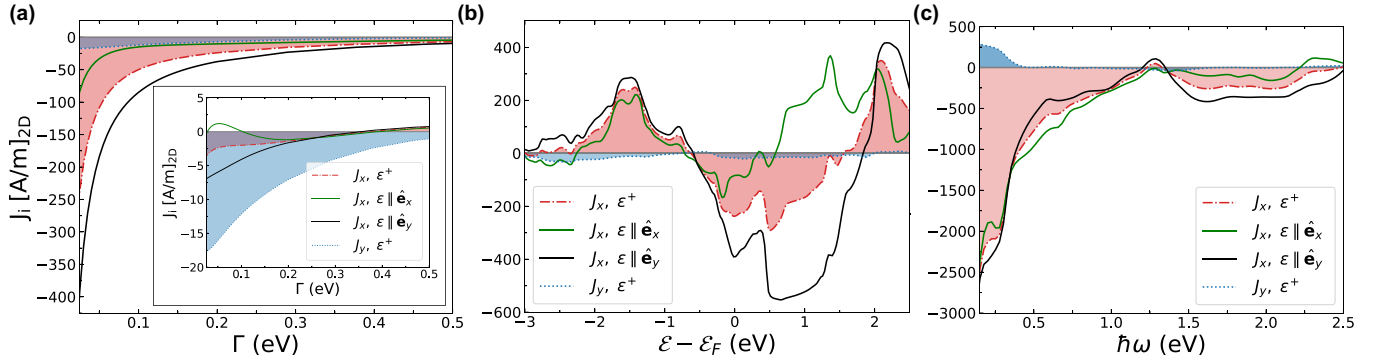


FIG. 2. Charge photocurrents in relation to (a) the lifetime broadening Γ , (b) the Fermi energy level \mathcal{E}_F , and (c) the frequency of light $\hbar\omega$ for the ferromagnetic BiAg₂ surface. The shown symmetry-allowed components are J_x for circularly polarized light (shaded dashed red line) and linearly polarized light along the x (green line) or y axis (black line), as well as J_y for circularly polarized light (shaded dotted blue line). The inset in (a) depicts only the three-band contributions to the ferromagnetic charge photocurrents, discussed in Sec. V. (a), (b) $\hbar\omega = 1.55$ eV; (b), (c) $\Gamma = 25$ meV. In (a), (c), the calculations are performed for true Fermi energy. For all calculations, the considered light intensity is $I = 10$ GW/cm². With ϵ^+ , we denote circularly polarized light with $\lambda = +1$ helicity, while with $\epsilon \parallel \hat{e}_x(\hat{e}_y)$, we denote linearly polarized light along $x(y)$.

IV. RESULTS

The results of our calculations and analysis regarding the charge and spin photocurrents are presented in the following section. In general, there is an agreement between the symmetry of the photocurrents that we observe from calculations and the symmetry restrictions derived from the effective Rashba model in Ref. [13]. For simplicity, we present the results only for the nonzero components allowed by symmetry. Furthermore, for circularly polarized light, we present only the results for the case of positive helicity $\lambda = +1$, while the case with $\lambda = -1$ can be reconstructed from the symmetry properties presented in [13].

A. Ferromagnetic charge photocurrents

We start by presenting in Fig. 2(a) the results of our calculations for the laser-induced charge photocurrents at the ferromagnetic BiAg₂ surface with in-plane magnetization along the y axis, in relation to the lifetime broadening of the electronic states Γ . The calculations are performed at the true Fermi energy level \mathcal{E}_F for a light frequency of $\hbar\omega = 1.55$ eV. We observe that the largest response arises for J_x from linearly polarized light along the y axis (black line) with a magnitude of nearly 400 A/m at $\Gamma = 25$ meV. The second largest response is for J_x driven by circularly polarized light (shaded dashed red line) with a magnitude of approximately 225 A/m at $\Gamma = 25$ meV. The remaining two types of photocurrent— J_x from light linearly polarized along the x axis (green line) and J_y from circularly polarized light (shaded dotted blue line)—are significantly smaller in magnitude, reaching a range of values from -25 to -75 A/m for small values of Γ .

We compare our results with previous experimental measurements of THz emission on ferromagnetic layers coupled to a Bi/Ag interface [46,47] and we find a symmetry agreement for the calculated large helicity independent J_x response (shaded dashed red line) and for the small helicity dependent J_y response (shaded dotted blue line). In comparison to

the results obtained from the effective ferromagnetic Rashba model as presented in Fig. 2 of Ref. [13], the values presented here are two orders of magnitude larger for the same laser pulse parameters. A possible source of this difference can lie in different values of the Rashba parameter used. In [13], a value of 0.1 eVÅ was used to model a Co/Pt magnetic bilayer, while for BiAg₂(111) surface alloys, the experimentally measured value is about 3.05 eVÅ [48]. This highlights the role of the interfacial Rashba SOI strength in generating surface photocurrents. Moreover, as we see in Fig. 2(a), the charge photocurrents decrease rapidly as the lifetime broadening Γ increases. For the values of Γ below 0.2 eV, photocurrents exhibit a highly nonlinear behavior, while for Γ above 0.2 eV, the latter behavior can be very well described by a $\sim \frac{1}{\Gamma}$ functional form. This kind of dependence of the photocurrents on the lifetime broadening was also recently observed for single-layer Fe₃GeTe₂ [16] by employing the same computational technique.

The magnitude and direction of the photocurrents also depend very strongly on the position of the Fermi energy. In Fig. 2(b), we present the results of calculated charge photocurrents as a function of the position of the Fermi energy in the electronic structure \mathcal{E}_F , while keeping $\Gamma = 25$ meV and $\hbar\omega = 1.55$ eV. Concerning the magnitude, generally similar behavior to that in Fig. 2(a) is observed, where the response of J_x to light with linear polarization along the y axis is the largest. An exception to this appears in the region of $[-1, +2]$ eV, where a change of sign occurs and the response of J_x for light with linear polarization along the x axis becomes dominant. Note that the J_y signal is strongly suppressed in the entire range of band filling. Qualitatively, the shape of the J_x response is similar for each case with the appearance of some pronounced variations which cause strong and sharp variations in the magnitude of the signal. Such variations can be noticed, for example, around -1.5 eV, around 0 eV, and around $+1.25$ eV. By comparing with the band structure presented in Fig. 1, we can identify these regions as the regions where bands become flatter or the number of participating in photocurrent bands increases. Therefore, when the Fermi

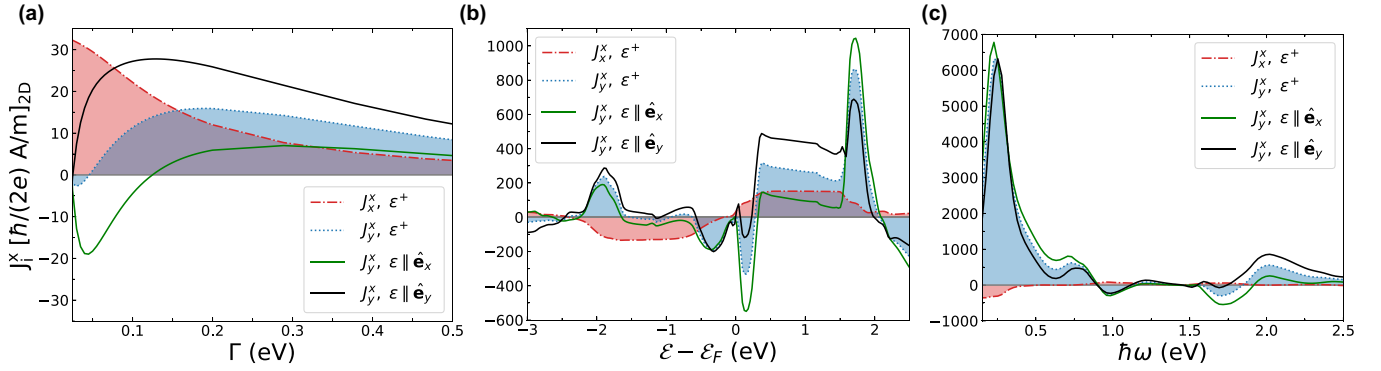


FIG. 3. Spin photocurrents in relation to (a) the lifetime broadening Γ , (b) the Fermi energy level \mathcal{E}_F , and (c) the light frequency $\hbar\omega$ for the nonmagnetic BiAg₂ surface. The symmetry-allowed components which are shown are the J_x^x for circularly polarized light (shadowed dashed red line), as well as J_y^x for circularly polarized light (shadowed dotted blue line) and linearly polarized light along the x (green line) or y (black line) axis. (a), (b) $\hbar\omega = 1.55$ eV; (b), (c) $\Gamma = 25$ meV. In (a), (c), the calculations are performed for the true Fermi energy. For all calculations, the considered light intensity is $I = 10$ GW/cm².

energy falls into these regions, the number of “activated” electronic transitions increases leading to increased magnitude of the photocurrents.

The dependence of charge photocurrents on the laser frequency $\hbar\omega$ is shown in Fig. 2(c). In this plot, the Fermi energy is set to the true Fermi level of BiAg₂, and a broadening of $\Gamma = 25$ meV is used. Concerning the magnitude of J_x , the resulting responses exhibit a nonlinear behavior in the region below 1.25 eV and a more stable behavior at higher frequencies. In general, the response for linearly polarized light along the y axis (black line) is the largest, except for the region of [0.5, 1.0] eV, where the response to linearly polarized light along the x axis (green line) becomes dominant. An interesting change of sign appears at an energy of around 1.25 eV for the J_x responses. The J_y response is, on the other hand, significant only in a relatively small frequency range around zero.

B. Nonmagnetic spin photocurrents

While the charge photocurrents are vanishing for nonmagnetic BiAg₂ due to symmetry, this is not the case for spin currents. We move on to present the results for the laser-induced spin photocurrents for the nonmagnetic BiAg₂ surface in Fig. 3. We present only the J_i^x responses with spin polarization along the x axis. The symmetry-allowed J_i^y responses arise as equal in magnitude and either the same or opposite in sign to J_i^x ones, and thus we omit them in the figure for simplicity. For circularly polarized light, J_x^x and J_y^y are the same, while J_y^x is opposite to J_x^y . For linearly polarized light, J_x^x polarized along x is opposite to J_x^y polarized along y , while J_x^x polarized along y is opposite to J_x^y polarized along x . The above relations are summarized in Table I.

In Fig. 3(a), the results with respect to the lifetime broadening Γ are presented. The calculations were performed at the true Fermi energy \mathcal{E}_F for the laser pulse frequency of $\hbar\omega = 1.55$ eV. For the J_x^x response for circularly polarized light (shadowed dashed red line), we observe the same behavior as in the case of charge photocurrents, i.e., nonlinear below 0.2 eV and more stable, $1/\Gamma$ -like, above 0.2 eV. At $\Gamma = 25$ meV, the calculated J_x^x has a magnitude of around

30 $\hbar/(2e)$ A/m. The J_y^x responses exhibit a different behavior. At small values of Γ , they converge to zero after reaching a peak value, while for larger values of Γ , they exhibit a steady $1/\Gamma$ behavior. The current response to circularly polarized light (shadowed dotted blue line) peaks at a magnitude of 15 $\hbar/(2e)$ A/m for $\Gamma \approx 0.2$ eV. In the case of linearly polarized light, for the polarization along x (green line), the peaked value is $-20 \hbar/(2e)$ A/m at $\Gamma \approx 50$ meV, while for polarization along y (black line), the peaked value is nearly 30 $\hbar/(2e)$ A/m at $\Gamma \approx 0.12$ eV.

The dependence of the spin photocurrents on the position of the Fermi energy \mathcal{E}_F in the nonmagnetic case is examined in Fig. 3(b) for $\hbar\omega = 1.55$ eV and Γ of 25 meV. As far as J_y^x current responses are concerned, their behavior is very similar for different light polarization cases. In contrast to charge photocurrents, the computed spin currents exhibit more pronounced peaks, which can be seen, for example, at ≈ -1.8 eV, $\approx +0.2$ eV, and $\approx +1.7$ eV. By comparing to the nonmagnetic band structure in Fig. 1, it is evident that these peaks originate from the regions where the bands become flatter or come closer, and where the number of electronic states lending themselves to optical transitions is increased. This feature is easier to distinguish in the nonmagnetic case as compared to the ferromagnetic one. In general, the response to light linearly polarized along y (black line) is the largest. An exception to this is observed in the regions where two more pronounced peaks appear in the response to light linearly polarized along x (green line). The J_x^x response to circularly polarized light (shadowed dashed red line) behaves differently

TABLE I. Relation between the symmetry-allowed J_i^x and J_i^y current responses of the spin photocurrents at nonmagnetic BiAg₂ surface. With ϵ^+ , we denote circularly polarized light with $\lambda = +1$ helicity, while with $\epsilon \parallel \hat{e}_x(\hat{e}_y)$, we denote linearly polarized light along $x(y)$.

$$\begin{aligned}
 J_x^x, \epsilon^+ &= J_y^y, \epsilon^+ \\
 J_y^x, \epsilon^+ &= -J_x^y, \epsilon^+ \\
 J_y^x, \epsilon \parallel \hat{e}_x &= -J_x^y, \epsilon \parallel \hat{e}_y \\
 J_x^x, \epsilon \parallel \hat{e}_y &= -J_y^y, \epsilon \parallel \hat{e}_x
 \end{aligned}$$

from the J_y^x . We can detect two regions, one below 0 eV, where the signal has a negative sign, and one above 0 eV, where the signal has a positive sign. In both cases, the signal reaches a steady value of about $200 \hbar/(2e)$ A/m for a wide range of nearly 1 eV.

The behavior of the spin photocurrents at the true Fermi level for a broadening of $\Gamma = 25$ meV in relation to the laser pulse frequency $\hbar\omega$ is depicted in Fig. 3(c). We can see that all J_y^x responses exhibit a similar behavior with a very sharp peak at ≈ 0.25 eV, while other peaks with smaller magnitude also arise as the laser frequency increases. By comparing with the nonmagnetic band structure in Fig. 1, it is straightforward to attribute these peaks to transitions at the band crossings which appear near ± 0.25 eV at the Γ and the K points, near +1 eV at the Γ point, near +1.75 eV at the Γ and the M points, and near -2 eV at the Γ point (see, also, discussion in Sec. V). The largest in magnitude responses arise for linearly polarized either along x (green line) or along y (black line) light. As far as the J_x^x response is concerned, it also exhibits peaks which correspond to the same transitions, although the response is around five times smaller in magnitude and opposite in sign.

C. Ferromagnetic spin photocurrents

The final case which we examine is that of laser-induced spin photocurrents for the ferromagnetic BiAg₂ surface. Their dependence concerning the lifetime broadening Γ at the true Fermi level and for a laser light frequency of $\hbar\omega = 1.55$ eV is presented in Figs. 4(a), 4(d) and 4(g). For values of Γ smaller than 0.25 eV, the behavior of J_i^x and J_i^y becomes nonlinear, while on the contrary, J_i^z reaches a peak value and slowly decreases to a finite value in the $\Gamma = 25$ meV limit of our computational capabilities. For the J_y^x response, the largest signal arises for linearly polarized along y light [black line in Fig. 4(a)], and for the J_x^x response, the largest signal arises for linearly polarized along x light [green line in Fig. 4(d)]. We also point out that J_x^x [shadowed dashed red line in Fig. 4(a)] and J_y^y [shadowed dotted blue line in Fig. 4(d)] current responses to circularly polarized light are rather suppressed in magnitude. Regarding the J_i^z currents, their magnitude is one order of magnitude smaller in comparison to J_i^x and J_i^y , with the largest signal appearing for the J_x^z response to circularly polarized light [shadowed dashed red line in Fig. 4(g)].

In Figs. 4(b), 4(e) and 4(h), we present the calculated spin photocurrents in response to variation of the Fermi energy \mathcal{E}_F for $\hbar\omega = 1.55$ eV and Γ of 25 meV. In general, we observe a larger magnitude of J_y^x current response, with J_x^x response being smaller by a factor of about two. In both cases, light linearly polarized along y [black line in Fig. 4(b) for J_y^x and black line in Fig. 4(e) for J_x^x] is the most optimal choice as it results in a larger signal for a wide range of energies. Also, for both cases, narrower regions where the response to light linearly polarized along x [green line in Fig. 4(b) for J_y^x and green line in Fig. 4(e) for J_x^x] becomes largest can be seen. Interestingly, for currents flowing in the direction of spin polarization, the response to circularly polarized light [shadowed dashed red line in Fig. 4(b) for J_x^x and shadowed dotted blue line in Fig. 4(e) for J_y^y] are suppressed in comparison to the J_y^x and J_x^x currents. As far as the J_i^z currents are concerned, their magnitude is one order of magnitude smaller than in

other cases. For all spin polarization directions, we observe that the shape of the curves is very ragged which makes it difficult to attribute given peaks to certain energy regions of the ferromagnetic band structure shown in Fig. 1. One can nevertheless notice that J_x^y and J_y^z currents have a similar shape with a change in sign despite their difference in magnitude.

We finally examine spin photocurrents as a function of the laser frequency, presenting the results in Figs. 4(c), 4(f) and 4(i). The calculation is once again performed at the true Fermi level \mathcal{E}_F for a lifetime broadening $\Gamma = 25$ meV. For all spin polarization directions, we notice that a very large peak appears near 0.25 eV and the behavior of the signals continues to be spiky at the same time decreasing in magnitude as the frequency increases. The peaks near 0.25 and 0.75 eV can be attributed to the band splittings which appear at the same energies of the ferromagnetic band structure shown in Fig. 1, i.e., near ± 0.25 eV and near ± 0.75 eV, at the Γ and K points, respectively, after the application of the exchange field. For selected parameters, J_y^x and J_x^y currents appear to be similar in magnitude, while J_i^z currents are one order of magnitude smaller. Also, once again, the J_x^x [shadowed dashed red line in Fig. 4(c)] and J_y^y [shadowed dotted blue line in Fig. 4(f)] responses to circular light are suppressed as compared to the others. In Fig. 4(c), the response of J_y^x to linearly polarized light along x (black line) is the largest, while in Fig. 4(f), the largest response of J_x^y occurs for linearly polarized light either along x (green line) or y (black line).

V. TWO-BAND VS THREE-BAND TRANSITIONS

In the last section, we perform an analysis of decomposition of the photocurrents into two-band and three-band contributions. In our notation, which follows the Keldysh nonequilibrium formalism, Eq. (2) involves a summation over three band indices— n, m, m' —originated from the expansion of three Green functions in the basis of Bloch states, given by Eq. (3). A resulting form of the corresponding expression can be seen in Eqs. (B4)–(B6) of Appendix B in Ref. [29]. In this context, the two-band transitions correspond to the case when $n = m$, while the three-band transitions correspond to the case when $n \neq m$. This is similar to the case considered in Refs. [20,49], where computed charge photocurrents are decomposed into two-band and three-band transitions between the energy bands within the second-order Kubo formalism [17]. The former kind of transitions can be considered as resonant transitions between two states that differ from each other by $\pm\hbar\omega$, and the latter as virtual transitions aided by a third band.

In the inset of Fig. 2(a), the contribution from the three-band transitions to the laser-induced charge photocurrents in the ferromagnetic BiAg₂ surface is shown. We find that for J_x currents, the two-band transitions dominate by one to two orders of magnitude, regardless of the light polarization. This finding is important since taking only two-band transitions into account reduces the computational effort significantly. Moreover, while we also find that two-band J_x currents are odd in the lifetime broadening Γ (i.e., odd in the relaxation time τ within the constant relaxation time approximation), the J_y response to circularly polarized light consists only of three-band transitions which are even in the lifetime

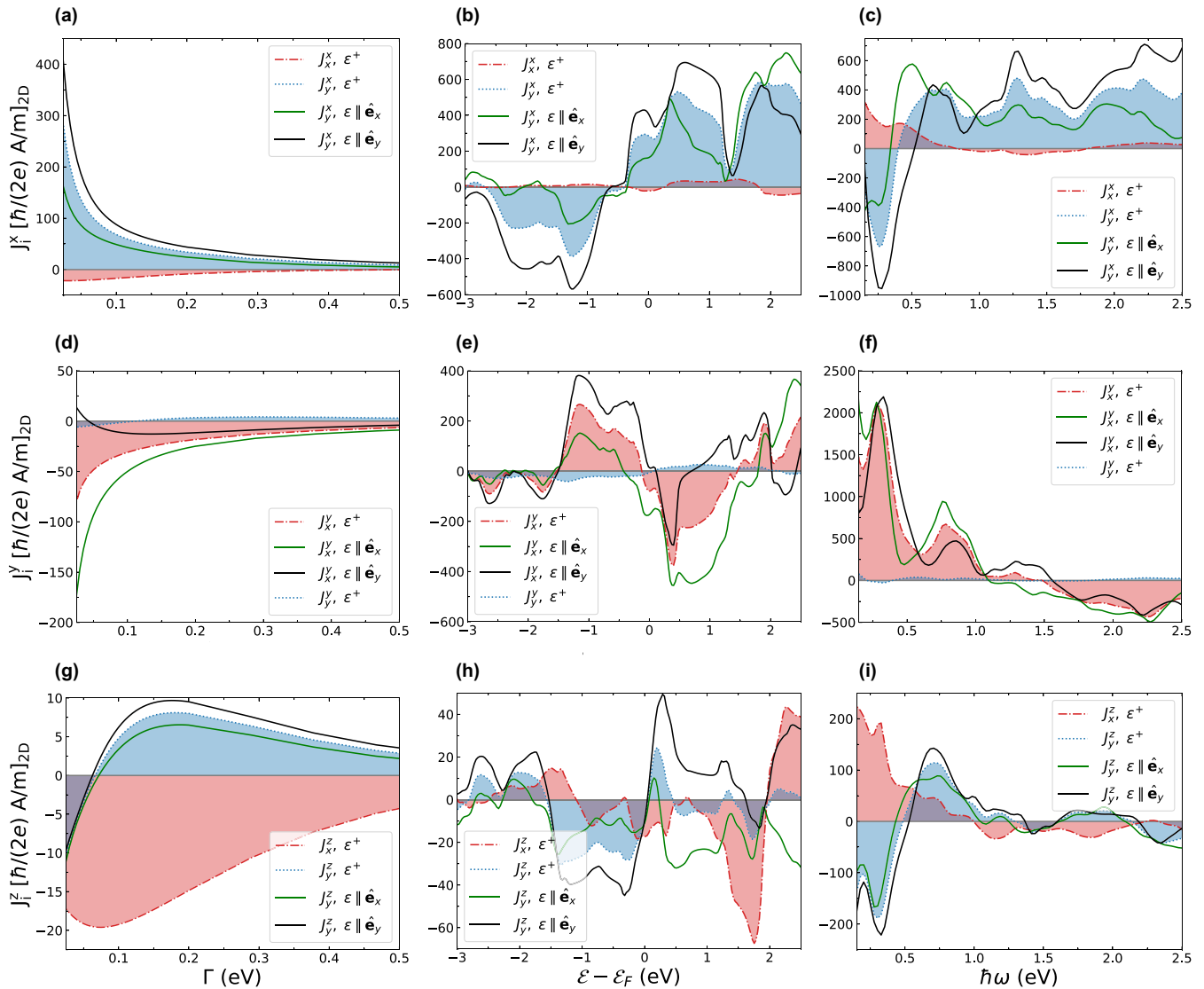


FIG. 4. Spin photocurrents in relation to (a), (d), (g) the lifetime broadening Γ , (b), (e), (h) the Fermi energy level \mathcal{E}_F , and (c), (f), (i) the light frequency $\hbar\omega$ for the ferromagnetic BiAg_2 surface. In (a)–(c), J_x^x and J_y^x with circularly polarized light (shadowed dashed red and shadowed dotted blue lines, respectively) together with J_y^x from linearly polarized along the x (green line) or y (black line) axis light are shown. In (d)–(f), J_x^y and J_y^y from circularly polarized light (shadowed dashed red and shadowed dotted blue lines, respectively) together with J_x^y from linearly polarized along the x (green line) or y (black line) axis light are shown. In (g)–(i), J_x^z and J_y^z from circularly polarized light (shadowed dashed red and shadowed dotted blue lines, respectively) together with J_y^z from linearly polarized along the x (green line) or y (black line) axis light are shown. In (a), (b), (d), (e), (g), (h), $\hbar\omega = 1.55$ eV, and in (b), (c), (e), (f), (h), (i), $\Gamma = 25$ meV. In (a), (c), (d), (f), (g), (i), the calculations are performed at the true Fermi energy level. For all calculations, the considered light intensity is $I = 10$ GW/cm².

broadening. Furthermore, in Figs. 5(a)–5(c), we present the spin photocurrents for the nonmagnetic case of the BiAg_2 surface, decomposed into two-band and three-band contributions. For the J_y^x current response, it is evident that both types of transitions contribute with similar magnitude to the resulting signal, and we also find that these currents are odd in the lifetime broadening Γ . On the contrary, J_x^x currents arising in response to circularly polarized light are driven exclusively by three-band transitions, exhibiting at the same time an even Γ dependence.

For the ferromagnetic spin photocurrents on the BiAg_2 surface, we present, in Figs. 5(d)–5(f), total, two-band, and three-band contributions, respectively, to J_i^x currents. Similarly to the ferromagnetic J_x charge photocurrents, we notice

that the two-band contribution is the most significant one for the J_y^x current responses. Comparing to the ferromagnetic J_x charge photocurrents, we find that three-band transitions are larger in this case, but still not important for the whole effect. In addition, we predict that J_y^x currents are odd in Γ . On the other hand, the response of J_x^x to circularly polarized light consists only of three-band transitions and it is even in Γ . The case for J_i^y (not shown) is similar to J_i^x with the J_x^x response mediated by two-band transitions and J_y^y current response to circularly polarized light mediated by three-band transitions, while being odd and even in Γ , respectively. Finally, all J_i^z currents comprise only three-band transitions, with the J_x^z being odd and J_y^z being even in Γ . The important conclusion that we can draw from our calculations is that in the case

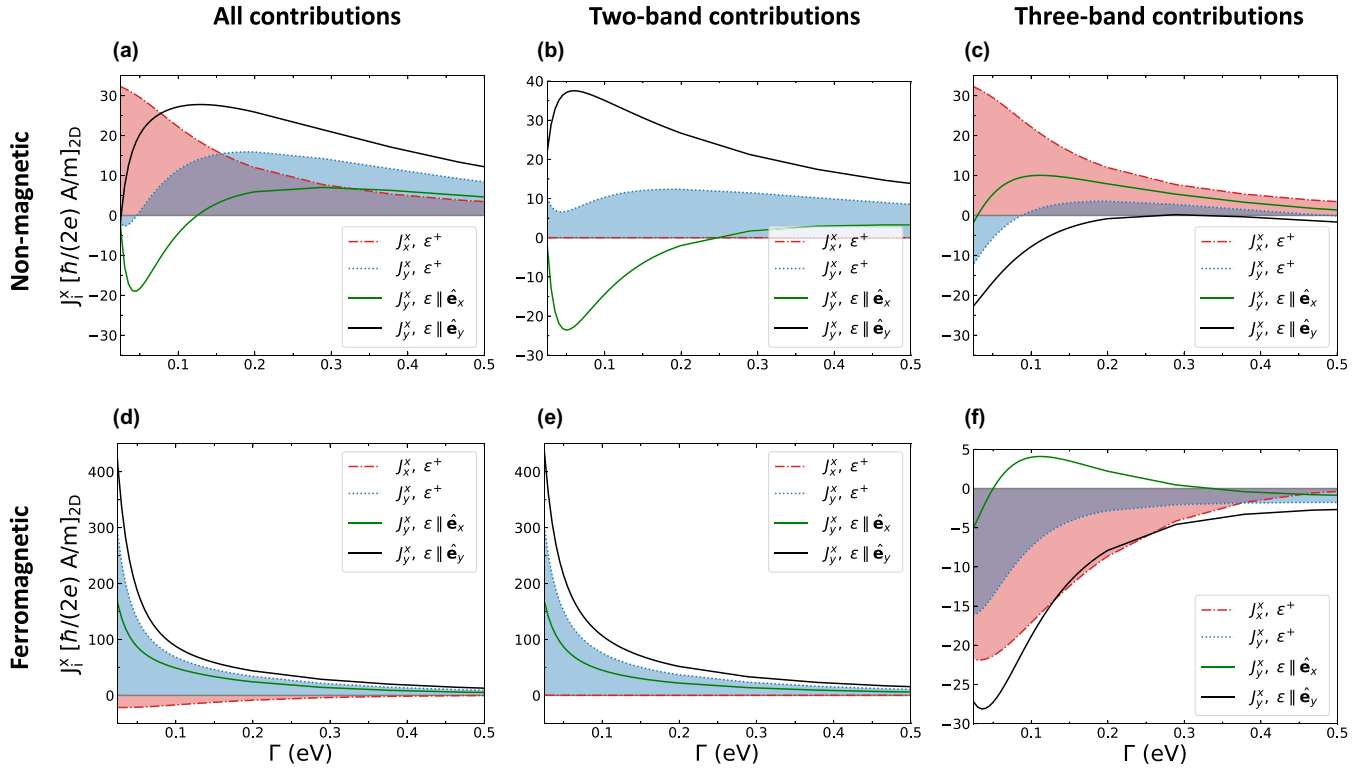


FIG. 5. Spin photocurrents in relation to the lifetime broadening Γ for the (a)–(c) nonmagnetic and the (d)–(f) ferromagnetic BiAg_2 surface. J_x^x and J_y^x with circularly polarized light (shadowed dashed red and shadowed dotted blue lines, respectively) together with J_y^x linearly polarized along the x (green line) or y (black line) axis are shown. In (a), (d), all the contributions to the spin photocurrents are presented, whereas in (b), (e), only the two-band and in (c), (f) only the three-band contributions are shown. For all cases, the calculations are performed at the true Fermi energy level with $\hbar\omega = 1.55$ eV. For all calculations, the considered light intensity is $I = 10$ GW/cm².

of spin currents, it is generally difficult to attribute a given component of the spin photocurrent to a specific type of band transitions without an in-depth analysis of the symmetry or explicit calculations.

In a last step, we calculate the band-resolved laser-induced charge and spin photocurrents for the ferromagnetic BiAg_2 surface by taking into account only the dominant contributions from the two-band transitions. The former is presented in Fig. 6(a) and the latter in Fig. 6(b). For both cases, we notice the appearance of “hot spots” where the magnitude of the photocurrents reaches large values as compared to the rest of the considered region where they vanish, while they are located within the energy region which is affected by the laser excitation, i.e., $[\mathcal{E}_f - \hbar\omega, \mathcal{E}_f + \hbar\omega]$. Moreover, we are able to classify the hot spots in pairs which are located at the same position in k space and their energy difference is equal to the energy of the laser pulse. These can be interpreted as two-band transitions which are generated by the laser excitation, as highlighted with numbered dashed red arrows in Fig. 6. We notice that these transitions are common both for charge and spin photocurrents, but only a few of them appear equally pronounced in both cases (see arrows 4, 7, and 9 in Fig. 6). On the other hand, there are transitions in which either the upper or the lower band appears pronounced (see arrows 3, 5, 6, and 8 in Fig. 6). There is also the case of transitions which are very prominent for the spin currents, but for the charge currents their magnitude is small (see arrows 1 and 2 in Fig. 6). For the charge photocurrents, the observed transitions either maintain

the sign of the photocurrents [see arrows 2 and 4 in Fig. 6(a)] or change it [see arrows 1, 3, and 5 in Fig. 6(a)]. In addition, no change of sign is observed for the spin photocurrents. In general, all the states participating in two-band transitions have predominantly Bi p character, thus making these states the only ones which contribute to the response effects in our system. This fact highlights even more the importance of the joint effect of Rashba and exchange splitting on the generation of the charge and spin photocurrents.

VI. SUMMARY

By using Keldysh formalism, we performed first-principles calculations of charge and spin photocurrents which arise as a second-order response to laser excitation at a BiAg_2 surface. We find that the calculated responses are large in magnitude and strongly depend on such material parameters as the lifetime broadening or the fine details of the electronic structure such as the position of the Fermi energy level and the laser pulse energy. These findings mark the surfaces and interfaces of strongly spin-orbit coupled materials as efficient sources not only of planar charge photocurrents, but also currents of spin, whose role in the processes of THz emission by spintronics systems has been possibly overlooked. Overall, our calculations for the experimentally well-studied BiAg_2 surface can be extremely useful for understanding the role of the interfacial Rashba spin-orbit interaction in generating various photocurrents. As such, our calculations can also serve

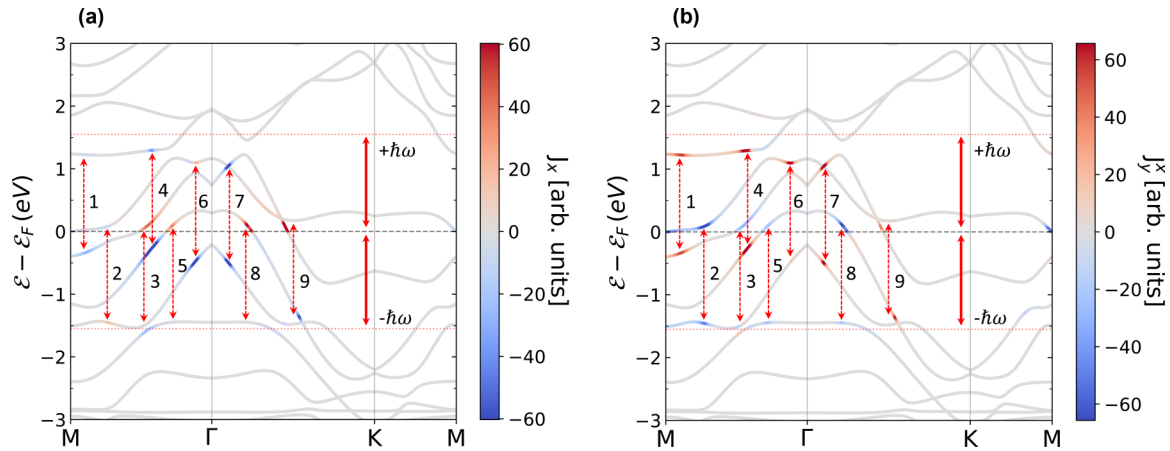


FIG. 6. Band-resolved two-band contributions of the laser-induced (a) charge and (b) spin photocurrents for the ferromagnetic BiAg_2 surface. Presented in (a) is the J_x response and in (b) is the J_y^s response, both for light linearly polarized along the x axis. The horizontal dotted red lines at ± 1.55 eV denote the energy of the laser pulse. The dashed red arrows depict two-band transitions between bands whose energy difference matches the laser pulse energy. In both cases, $\hbar\omega = 1.55$ eV and $\Gamma = 25$ meV. Throughout the calculations, the considered light intensity is $I = 10$ GW/cm 2 .

as a benchmark for further material-specific studies of photoinduced charge and spin dynamics.

ACKNOWLEDGMENTS

This work was supported by the Deutsche Forschungsgemeinschaft (DFG, German Research Foundation), TRR 173/2 - 268565370 (Project No. A11) and TRR 288

- 422213477 (Project No. B06), and the Sino-German research project DISTOMAT (Grant No. MO 1731/10-1). This project has received funding from the European Union's Horizon 2020 research and innovation programme under the Marie Skłodowska-Curie Grant Agreement No. 861300. We also gratefully acknowledge the Jülich Supercomputing Centre and RWTH Aachen University for providing computational resources under Projects No. jiff40 and No. jara0062.

- [1] T. Seifert, S. Jaiswal, U. Martens, J. Hannegan, L. Braun, P. Maldonado, F. Freimuth, A. Kronenberg, J. Henrzi, I. Radu, E. Beaupaire, Y. Mokrousov, P. M. Oppeneer, M. Jourdan, G. Jakob, D. Turchinovich, L. M. Hayden, M. Wolf, M. Münzenberg, M. Kläui *et al.*, Efficient metallic spintronic emitters of ultrabroadband terahertz radiation, *Nat. Photon.* **10**, 483 (2016).
- [2] E. T. Papaioannou and R. Beigang, THz spintronic emitters: a review on achievements and future challenges, *Nanophotonics* **10**, 1243 (2021).
- [3] T. Kampfrath, M. Battiato, P. Maldonado, G. Eilers, J. Nötzold, S. Mährlein, V. Zbarsky, F. Freimuth, Y. Mokrousov, S. Blügel, M. Wolf, I. Radu, P. M. Oppeneer, and M. Münzenberg, Terahertz spin current pulses controlled by magnetic heterostructures, *Nat. Nanotechnol.* **8**, 256 (2013).
- [4] T. J. Huisman, C. Ciccirelli, A. Tsukamoto, R. V. Mikhaylovskiy, T. Rasing, and A. V. Kimel, Spin-photocurrents generated by femtosecond laser pulses in a ferrimagnetic GdFeCo/Pt bilayer, *Appl. Phys. Lett.* **110**, 072402 (2017).
- [5] M. Battiato, K. Carva, and P. M. Oppeneer, Superdiffusive Spin Transport as a Mechanism of Ultrafast Demagnetization, *Phys. Rev. Lett.* **105**, 027203 (2010).
- [6] M. Battiato, K. Carva, and P. M. Oppeneer, Theory of laser-induced ultrafast superdiffusive spin transport in layered heterostructures, *Phys. Rev. B* **86**, 024404 (2012).
- [7] G. Malinowski, F. Dalla Longa, J. H. H. Rietjens, P. V. Paluskar, R. Huijink, H. J. M. Swagten, and B. Koopmans, Control of speed and efficiency of ultrafast demagnetization by direct transfer of spin angular momentum, *Nat. Phys.* **4**, 855 (2008).
- [8] A. Melnikov, I. Razdolski, T. O. Wehling, E. T. Papaioannou, V. Roddatis, P. Fumagalli, O. Aktsipetrov, A. I. Lichtenstein, and U. Bovensiepen, Ultrafast Transport of Laser-Excited Spin-Polarized Carriers in Au/Fe/MgO(001), *Phys. Rev. Lett.* **107**, 076601 (2011).
- [9] T. J. Huisman, R. V. Mikhaylovskiy, J. D. Costa, F. Freimuth, E. Paz, J. Ventura, P. P. Freitas, S. Blügel, Y. Mokrousov, T. Rasing, and A. V. Kimel, Femtosecond control of electric currents in metallic ferromagnetic heterostructures, *Nat. Nanotechnol.* **11**, 455 (2016).
- [10] G.-M. Choi, A. Schleife, and D. G. Cahill, Optical-helicity-driven magnetization dynamics in metallic ferromagnets, *Nat. Commun.* **8**, 15085 (2017).
- [11] F. Freimuth, S. Blügel, and Y. Mokrousov, Direct and inverse spin-orbit torques, *Phys. Rev. B* **92**, 064415 (2015).
- [12] F. Freimuth, S. Blügel, and Y. Mokrousov, Charge pumping driven by the laser-induced dynamics of the exchange splitting, *Phys. Rev. B* **95**, 094434 (2017).
- [13] F. Freimuth, S. Blügel, and Y. Mokrousov, Charge and spin photocurrents in the Rashba model, *Phys. Rev. B* **103**, 075428 (2021).
- [14] S. D. Ganichev and W. Prettl, Spin photocurrents in quantum wells, *J. Phys.: Condens. Matter* **15**, R935 (2003).
- [15] Q. Ma, S.-Y. Xu, C.-K. Chan, C.-L. Zhang, G. Chang, Y. Lin, W. Xie, T. Palacios, H. Lin, S. Jia, P. A. Lee, P. Jarillo-Herrero,

- and N. Gedik, Direct optical detection of Weyl fermion chirality in a topological semimetal, *Nat. Phys.* **13**, 842 (2017).
- [16] M. Merte, F. Freimuth, T. Adamantopoulos, D. Go, T. G. Saunderson, M. Kläui, L. Plucinski, O. Gomonay, S. Blügel, and Y. Mokrousov, Photocurrents of charge and spin in monolayer Fe_3GeTe_2 , *Phys. Rev. B* **104**, L220405 (2021).
- [17] R. von Baltz and W. Kraut, Theory of the bulk photovoltaic effect in pure crystals, *Phys. Rev. B* **23**, 5590 (1981).
- [18] J. E. Sipe and A. I. Shkrebti, Second-order optical response in semiconductors, *Phys. Rev. B* **61**, 5337 (2000).
- [19] J. Ibanez-Azpiroz, S. S. Tsirkin, and I. Souza, *Ab initio* calculation of the shift photocurrent by Wannier interpolation, *Phys. Rev. B* **97**, 245143 (2018).
- [20] Y. Zhang, H. Ishizuka, J. van den Brink, C. Felser, B. Yan, and N. Nagaosa, Photogalvanic effect in Weyl semimetals from first principles, *Phys. Rev. B* **97**, 241118(R) (2018).
- [21] I. Sodemann and L. Fu, Quantum Nonlinear Hall Effect Induced by Berry Curvature Dipole in Time-Reversal Invariant Materials, *Phys. Rev. Lett.* **115**, 216806 (2015).
- [22] O. Matsyshyn and I. Sodemann, Nonlinear Hall Acceleration and the Quantum Rectification Sum Rule, *Phys. Rev. Lett.* **123**, 246602 (2019).
- [23] B. M. Fregoso, R. A. Muniz, and J. E. Sipe, Jerk Current: A Novel Bulk Photovoltaic Effect, *Phys. Rev. Lett.* **121**, 176604 (2018).
- [24] B. M. Fregoso, Bulk photovoltaic effects in the presence of a static electric field, *Phys. Rev. B* **100**, 064301 (2019).
- [25] B. I. Sturman, Ballistic and shift currents in the bulk photovoltaic effect theory, *Phys. Usp.* **63**, 407 (2020).
- [26] X. Mu, Y. Pan, and J. Zhou, Pure bulk orbital and spin photocurrent in two-dimensional ferroelectric materials, *npj Comput. Mater.* **7**, 61 (2021).
- [27] E. Y. Sherman, A. Najmaie, and J. E. Sipe, Spin current injection by intersubband transitions in quantum wells, *Appl. Phys. Lett.* **86**, 122103 (2005).
- [28] J. Yin and H. Peng, Asymmetry allows photocurrent in intrinsic graphene, *Nat. Nanotechnol.* **14**, 105 (2019).
- [29] F. Freimuth, S. Blügel, and Y. Mokrousov, Laser-induced torques in metallic ferromagnets, *Phys. Rev. B* **94**, 144432 (2016).
- [30] H. Xu, H. Wang, J. Zhou, and J. Li, Pure spin photocurrent in non-centrosymmetric crystals: bulk spin photovoltaic effect, *Nat. Commun.* **12**, 4330 (2021).
- [31] R.-C. Xiao, D.-F. Shao, Y.-H. Li, and H. Jiang, Spin photogalvanic effect in two-dimensional collinear antiferromagnets, *npj Quantum Mater.* **6**, 35 (2021).
- [32] S. Hayami, M. Yatsushiro, and H. Kusunose, Nonlinear spin Hall effect in \mathcal{PT} -symmetric collinear magnets, *Phys. Rev. B* **106**, 024405 (2022).
- [33] R. Fei, W. Song, L. Pusey-Nazzaro, and L. Yang, \mathcal{PT} -Symmetry-Enabled Spin Circular Photogalvanic Effect in Antiferromagnetic Insulators, *Phys. Rev. Lett.* **127**, 207402 (2021).
- [34] H. Kurebayashi, J. H. Garcia, S. Khan, J. Sinova, and S. Roche, Magnetism, symmetry and spin transport in van der Waals layered systems, *Nat. Rev. Phys.* **4**, 150 (2022).
- [35] M. A. Wahada, E. Şaşıoğlu, W. Hoppe, X. Zhou, H. Deniz, R. Rouzegar, T. Kampfrath, I. Mertig, S. S. P. Parkin, and G. Woltersdorf, Atomic scale control of spin current transmission at interfaces, *Nano Lett.* **22**, 3539 (2022).
- [36] K. S. Burch, D. Mandrus, and J.-G. Park, Magnetism in two-dimensional van der Waals materials, *Nature (London)* **563**, 47 (2018).
- [37] T. Schumann, T. Kleinke, L. Braun, N. Meyer, G. Mussler, J. Kampmeier, D. Grützmacher, E. Schmoranzero, K. Olejník, H. Reichlová, C. Heiliger, C. Denker, J. Walowski, T. Kampfrath, and M. Münzenberg, Circular photogalvanic effects in topological insulator/ferromagnet hybrid structures (unpublished).
- [38] C. Carbone, P. Moras, P. M. Sheverdyeva, D. Pacilé, M. Papagno, L. Ferrari, D. Topwal, E. Vescovo, G. Bihlmayer, F. Freimuth, Y. Mokrousov, and S. Blügel, Asymmetric band gaps in a Rashba film system, *Phys. Rev. B* **93**, 125409 (2016).
- [39] www.flapw.de.
- [40] C. Li, A. J. Freeman, H. J. F. Jansen, and C. L. Fu, Magnetic anisotropy in low-dimensional ferromagnetic systems: Fe monolayers on Ag(001), Au(001), and Pd(001) substrates, *Phys. Rev. B* **42**, 5433 (1990).
- [41] J. P. Perdew, K. Burke, and M. Ernzerhof, Generalized Gradient Approximation Made Simple, *Phys. Rev. Lett.* **77**, 3865 (1996).
- [42] D. Go, J.-P. Hanke, P. M. Buhl, F. Freimuth, G. Bihlmayer, H.-W. Lee, Y. Mokrousov, and S. Blügel, Toward surface orbitronics: giant orbital magnetism from the orbital Rashba effect at the surface of *sp*-metals, *Sci. Rep.* **7**, 46742 (2017).
- [43] G. Pizzi, V. Vitale, R. Arita, S. Blügel, F. Freimuth, G. Géranton, M. Gibertini, D. Gresch, C. Johnson, T. Koretsune, J. Ibañez-Azpiroz, H. Lee, J.-M. Lihm, D. Marchand, A. Marrazzo, Y. Mokrousov, J. I. Mustafa, Y. Nohara, Y. Nomura, L. Paulatto *et al.*, Wannier90 as a community code: new features and applications, *J. Phys.: Condens. Matter* **32**, 165902 (2020).
- [44] H. Zhang, F. Freimuth, G. Bihlmayer, S. Blügel, and Y. Mokrousov, Topological phases of Bi(111) bilayer in an external exchange field, *Phys. Rev. B* **86**, 035104 (2012).
- [45] F. R. Lux, F. Freimuth, S. Blügel, and Y. Mokrousov, Engineering chiral and topological orbital magnetism of domain walls and skyrmions, *Commun. Phys.* **1**, 60 (2018).
- [46] M. B. Jungfleisch, Q. Zhang, W. Zhang, J. E. Pearson, R. D. Schaller, H. Wen, and A. Hoffmann, Control of Terahertz Emission by Ultrafast Spin-Charge Current Conversion at Rashba Interfaces, *Phys. Rev. Lett.* **120**, 207207 (2018).
- [47] C. Zhou, Y. P. Liu, Z. Wang, S. J. Ma, M. W. Jia, R. Q. Wu, L. Zhou, W. Zhang, M. K. Liu, Y. Z. Wu, and J. Qi, Broadband Terahertz Generation via the Interface Inverse Rashba-Edelstein Effect, *Phys. Rev. Lett.* **121**, 086801 (2018).
- [48] C. R. Ast, J. Henk, A. Ernst, L. Moreschini, M. C. Falub, D. Pacilé, P. Bruno, K. Kern, and M. Grioni, Giant Spin Splitting through Surface Alloying, *Phys. Rev. Lett.* **98**, 186807 (2007).
- [49] Y. Zhang, T. Holder, H. Ishizuka, F. de Juan, N. Nagaosa, C. Felser, and B. Yan, Switchable magnetic bulk photovoltaic effect in the two-dimensional magnet CrI_3 , *Nat. Commun.* **10**, 3783 (2019).